



Cite this: *Analyst*, 2023, **148**, 2045

# Synthesis and characterization of a fluorescent polymeric nano-thermometer: dynamic monitoring of 3D temperature distribution in co-cultured tumor spheroids†

Ashish Kumar,<sup>‡a</sup> Venkanagouda S. Goudar,<sup>‡a</sup> Kiran Kaladharan,<sup>a</sup>  
Tuhin Subhra Santra <sup>b</sup> and Fan-Gang Tseng <sup>\*a,c,d,e</sup>

Temperature governs the reactivity of a wide range of biomolecules in the cellular environment dynamically. The complex cellular pathways and molecules in solid tumors substantially produce temperature gradients in the tumor microenvironment (TME). Hence, visualization of these temperature gradients at the cellular level would give physiologically relevant spatio-temporal information about solid tumors. This study used fluorescent polymeric nano-thermometers (FPNTs) to measure the intratumor temperature in co-cultured 3D tumor spheroids. A temperature-sensitive rhodamine-B dye and Pluronic F-127 were conjugated through hydrophobic and hydrophobic interactions and then cross-linked with urea–paraformaldehyde resins to form the FPNTs. The characterization results exhibit monodisperse nanoparticles ( $166 \pm 10$  nm) with persistent fluorescence. The FPNTs exhibit a linear response with a wide temperature sensing range (25–100 °C) and are stable toward pH, ionic strength, and oxidative stress. FPNTs were utilized to monitor the temperature gradient in co-cultured 3D tumor spheroids and the temperature difference between the core (34.9 °C) and the periphery (37.8 °C) was 2.9 °C. This investigation demonstrates that the FPNTs have great stability, biocompatibility, and high intensity in a biological medium. The usage of FPNTs as a multifunctional adjuvant may demonstrate the dynamics of the TME and they may be suitable candidates to examine thermoregulation in tumor spheroids.

Received 1st December 2022,  
Accepted 26th February 2023

DOI: 10.1039/d2an01968j

rsc.li/analyst

## 1. Introduction

Temperature is an essential physiological parameter that governs the dynamics of equilibrium constants and the reactivity of a wide range of biochemical kinetics (exothermic and endothermic reactions) such as gene expression, protein stability, enzyme–ligand interactions, and enzyme activity in living organisms.<sup>1</sup> These exothermic and endothermic reactions

cause temperature changes within the cells and might be affected by local temperature fluctuations.<sup>2,3</sup> Thus, accurate temperature measurement is essential in cells and their surrounding environment. Cancer cells within tumors have higher temperatures than normal cells due to their different metabolic rates, which are particularly important in cancer progression. Cancer cells of non-Hodgkin lymphoma have higher temperatures, which is associated with increased malignancy and poor patient survival.<sup>3</sup> Interestingly, in the case of breast cancer, a 3.5 °C higher temperature was noticed in comparison with the surrounding healthy tissue.<sup>4</sup> Subsequently, pathological investigations have revealed that temperature is correlated with disease advancement and cellular activity in cancer. Moreover, the tumor microenvironment of each type of tumor depends on its chemical behavior; for example, the balance of cytokines, angiogenesis factors, and growth factors defines the temperature gradient in each type of cancer. Particularly, hypoxia is known to reduce the temperature and induce the synthesis of stress hormones, and activate different pro-cancer pathways. All of these together have an impact on cancer progression, metastasis, poor prognosis, and drug resistance in several cancers.<sup>3,5–8</sup> Until now, there have been no

<sup>a</sup>Department of Engineering and System Science, National Tsing Hua University, Hsinchu, 30013, Taiwan ROC. E-mail: fangang@ess.nthu.edu.tw, fangangtseng@gmail.com, aashu9t@gapp.nthu.edu.tw, raiaash024@gmail.com, venkatesh.gdr22@gmail.com, kiran.911989@gmail.com

<sup>b</sup>Department of Engineering Design, Indian Institute of Technology Madras, Chennai, 600036, India. E-mail: santra.tuhin@gmail.com, tuhin@iitm.ac.in

<sup>c</sup>Institute of Nano Engineering and Microsystems, National Tsing Hua University, Hsinchu, 30013, Taiwan ROC

<sup>d</sup>Research Center for Applied Sciences, Academia Sinica, Taipei, 11529, Taiwan ROC

<sup>e</sup>Frontier Research Center on Fundamental and Applied Sciences of Matters, National Tsing Hua University, Hsinchu, 30013 Taiwan, Republic of China

†Electronic supplementary information (ESI) available. See DOI: <https://doi.org/10.1039/d2an01968j>

‡These authors contributed equally to this work.

clear shreds of evidence or mechanisms on how temperature variations orchestrate the biochemical reactions during cancer progression and tumorigenesis. Thus, collecting the data that omit the patterns of temperature variations at the subcellular level in the native tumor environment could reveal physiologically relevant spatio-temporal information on metabolism. However, conventional thermo-sensing methodologies such as thermocouples and more fail to measure the localized temperature dynamically within a small confined area.<sup>9–11</sup> In this regard, modern requirements for temperature monitoring have led to the development of noninvasive nanothermometers.<sup>12–14</sup> Such noninvasive nanothermometers would enable thermometry with a precision that would be hardly achieved by conventional or invasive methods.<sup>15–17</sup> Among the various nanothermometers, fluorescence-based thermal sensors have shown considerable advantages due to their high temporal and spatial resolution and the capability of “non-contact” tools for both imaging and temperature sensing simultaneously.<sup>18–23</sup> There have been several different types of fluorescence-based temperature sensors developed over the past few decades, including semiconductor quantum dots,<sup>13,23–26</sup> rare earth metal doped nanoparticles,<sup>22,23,27</sup> carbon dots,<sup>28–30</sup> and metal nanoclusters (MNCs).<sup>4,31–33</sup> Interestingly, Suzuki *et al.* and Gao *et al.* developed a glass micropipette loaded with a thermo-sensitive fluorescent dye thenoyltrifluoroacetate trihydrate (Eu-TTA-Europium (III)) and oil dispersible AIEgen and butter-based nano-thermometer respectively to measure the cellular temperature<sup>30,34</sup> Yang *et al.* reported quantum dot-based sensors to measure the local temperature response to external chemical and physical stimulations.<sup>31</sup> However, polymeric materials used to prepare fluorescence-based sensors are more likely to suffer from thermostability. For example, nano-gels prepared with green fluorescent protein (GFP) sensors can sense  $\pm 15$  °C around the transition temperature of the gel.<sup>35</sup> Sensors developed with QDs and silicon nanoparticles can sense temperatures of 20–40 °C and 0–60 °C, respectively.<sup>36</sup> Though some of the fluorescent molecules were prepared with inorganic materials, their temperature could range from 50 to 300 K; however, they need to be excited by ultraviolet light,<sup>37</sup> which might lead to a strong background and toxicity. Thus, the aforementioned materials have some drawbacks such as a small temperature range, systematic errors, bio-toxicity, environmental contamination, and unstable optical characteristics in various circumstances. As a result, these constraints make them incompatible with different biological and biomedical applications.<sup>34,38,39</sup>

Thus, fluorescent particles with stable accuracy, a broad sensing range, particular excitation and emission, and decent biocompatibility are essential for fluorescence-based temperature sensors. Out of many organic fluorophores, Rh-B dyes show high quantum yields, strong fluorescence emission, and stable temperature sensing properties and they can be used for various sensing and temperature sensing applications.<sup>40</sup> In particular, the fluorescence intensity of Rh-B decreases as the temperature increases.<sup>41–43</sup> However, the Rh-dyes are toxic;

hence, the effective and lethal doses (ED-50 and LD-50) of Rh-B's range between 14 and 24 mg L<sup>−1</sup> for aquatic creatures' life (algae, fish embryos, *etc.*).<sup>41,42</sup> The maximum acceptable concentrations of Rh-B for aquatic life (MAC-QS) and annual average quality standard (AA-QS) were found to be 14 and 140 g L<sup>−1</sup>, respectively.<sup>42</sup> On the other hand, the Rh-B dye encapsulated in nano-carriers by precipitation and electrospray methods exhibits high dye leakage, and these particles could not meet the criteria of temperature sensing applications.<sup>43</sup> Thus recently, polymeric nanoparticle (NP)-based temperature sensors have attracted a surge of interest because of the unique features that come with their small size, transparency, and excellent biocompatibility.<sup>44–46</sup> In this context, F-127, a surfactant, the triblock copolymer has been used to form dye-micelle complexes in various biomedical applications.<sup>47</sup> Moreover, Pluronic F-127 was reported to have long hydrophilic chains and exhibit prominent hydrophilic nature in solution.<sup>48</sup>

On the other hand, melamine-formaldehyde (MF) and urea-formaldehyde (UPF), which are amino resins with strongly cross-linked internal structures, have been widely used as crosslinking agents in fluorescent materials synthesis and encapsulation.<sup>49–51</sup> Pluronic F-127 was also used as a surfactant to prepare resorcinol-formaldehyde and melamine-formaldehyde nanoparticles.<sup>52</sup> Previous studies used the sol-gel process to synthesize homogeneous polymer nanoparticles.<sup>53</sup> Sol-to-gel transitions in aqueous Pluronic solutions were known to occur through a shift from unimers to micelles.<sup>47</sup> These dye-micelle complexes were incorporated into previously formed MF nanoparticles.<sup>54</sup>

In this study, we developed a fluorescent polymeric nanothermometer (FPNT) in three steps to quantify intratumor temperature distribution in co-cultured *in vitro* 3D tumor spheroids. As shown in Fig. 1, urea-formaldehyde particles were prepared as in a previous method,<sup>55</sup> and a Rh-B dye-surfactant micelle was prepared. Furthermore, the dye-incorporated micelle was polymerized with UPF particles at high temperatures under acid catalysis, which leads to an enhancement in the cross-linking of internal structures, stabilizing the encapsulation and leakage of the fluorescent dye from the fabricated FPNTs. Finally, ~166 nm FPNTs were used to study the temperature sensing in an *in vitro* co-cultured 3D tumor spheroid. Here, we investigated the temperature dependence and reversibility of the FPNTs from 25 to 100 °C. Finally, fluorescence confocal microscopy was used to reveal 3D temperature distribution dynamically in the 3D co-cultured tumor spheroids. It was shown that FPNTs might be used as nanothermometers across a wide temperature range for hyperthermia process monitoring inside tumor microenvironments.

## 2. Materials and methods

### 2.1 Materials

All the materials and chemicals are mentioned in ESI section 1.1.†

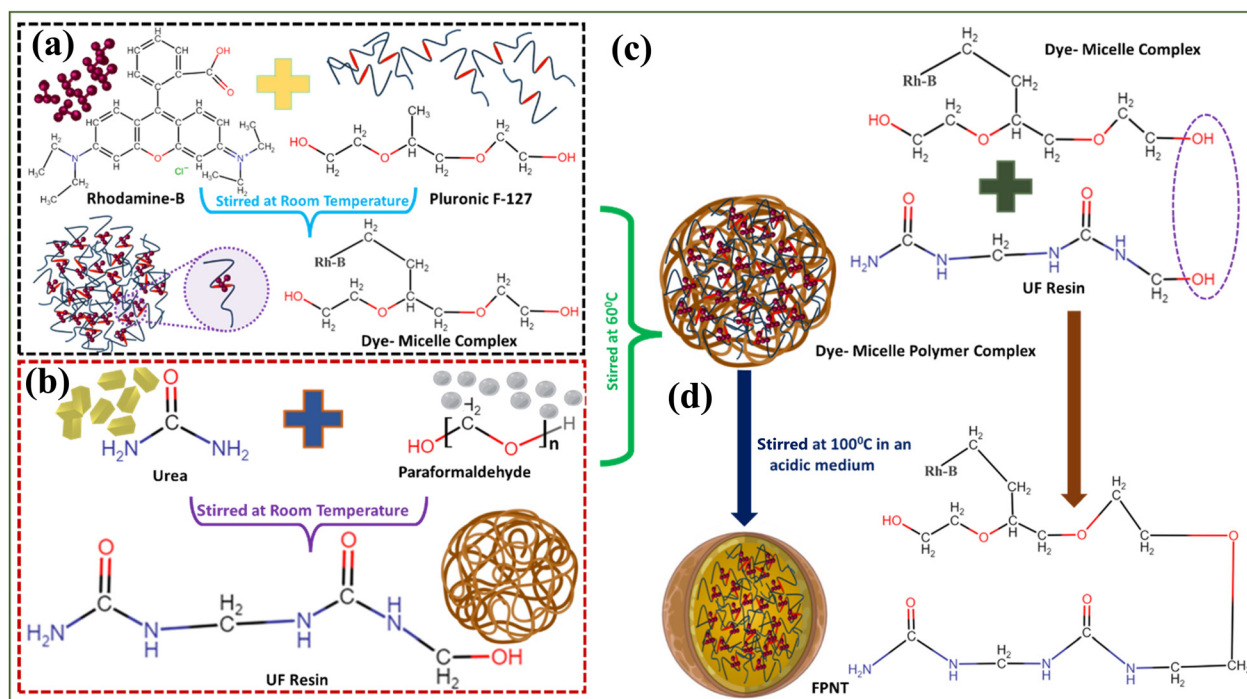


**Fig. 1** Schematic illustration of the preparation of FPNTs. (a) Micelle formation of the Rh-B dye and Pluronic F-127 polymer by a hydrophobic and hydrophobic interaction mechanism. (b) Formation of a urea and paraformaldehyde resin, which acts as a cross-linker. (c) Incorporation of a dye micelle in UF resin. (d) Condensation of the hydroxyl group results in FPNTs.

## 2.2 Preparation of fluorescent polymeric nano-thermometers (FPNTs)

A three-step procedure, as shown in Fig. 1, was used to create polymeric particles with Rh-B. First, Pluronic F-127 and the Rh-B dye were blended in DI water for 2.5–3 hours at 27 °C to form a dye-micelle complex. Following the completion of the first step, urea and paraformaldehyde were added to prepare a dye-micelle polymer complex (DMPC). Finally, hydrochloric acid was added to obtain an acidic pH ( $\sim$ pH 3), and the mixture was heated in a boiling water bath to allow the synthesis and cross-linking of polymeric nano-thermometers (FPNTs). The detailed description is represented in ESI section 1.2.†

## 2.3 Characterization of FPNTs

Scanning electron microscopy (SEM) and dynamic light scattering (DLS) measurements were used to determine the size of the FPNTs. Fourier-transform infrared (FTIR) spectroscopy and  $^1\text{H}$  nuclear magnetic resonance ( $^1\text{H}$  NMR) analyses were used to measure the bonding characteristics and molecular structures present in the FPNTs. Fluorescence spectroscopy was used to measure the intensity variations of the FPNTs. The detailed sample preparation procedures and specifications are mentioned in ESI section 1.3.†

## 2.4 Fabrication of the PDMS temperature calibration (PTC) chip

For temperature calibration, PTC comprises three layers: glass–PDMS–glass substrate, as shown in ESI Fig. S1.† The prepared

PDMS was poured onto a pre-cleaned silicon wafer and cured at 80 °C for two hours. Later, PDMS was progressively peeled away, and arrays of macro-wells were created. Furthermore, PDMS was cleaned and bonded to the bottom glass substrate and the top glass slide was kept detached. The detailed fabrication process is presented in ESI section 1.4.†

## 2.5 Temperature-dependent fluorescence intensity calibration of FPNTs on a PTC chip

The experimental setup and calibration process of temperature-dependent fluorescence intensity calibration of the FPNTs are presented in ESI section 1.5.†

## 2.6 Open $\mu$ -well 3D cell culture chip design and fabrication

An open  $\mu$ -well 3D cell-culture platform was created to co-culture the cancer and fibroblast cell lines to form multicellular spheroids.<sup>56</sup> The detailed chip design and fabrication process of the open  $\mu$ -well 3D cell culture platform is presented in ESI section 1.6.†

## 2.7 Determination of the half-maximal inhibitory concentration ( $\text{IC}_{50}$ ) on 2D cultures

HCT-8 and NIH3T3 cells were used in this study and were obtained from the Bioresource Collection and Research Center (BCRC) in Hsinchu, Taiwan. HCT-8 and NIH3T3 cells were initially seeded with approximately 3000 cells per well in a complete growth medium. Furthermore, the prepared FPNTs were mixed uniformly in PBS solution and added individually

to each well of the 96-well plates with final concentrations of 100, 50, 25, 10, 5, 1, 0.1, 0.01, and 0.001  $\mu\text{M}$  in the cell culture medium. The detailed procedure for the determination of the half-maximal inhibitory concentration of FPNTs is presented in ESI section 1.7.†

### 2.8 *In vitro* 3D co-culture on an open $\mu$ -well 3D cell culture chip

Cancer cell lines (HCT-8) and fibroblast cell lines (NIH3T3) were used to co-culture and form multicellular spheroids. The detailed procedure of spheroid formation is described in ESI section 1.8.†

### 2.9 Dynamic temperature measurement inside the 3D co-cultured tumor spheroids

FPNTs were used to measure the temperature inside the 3D co-cultured tumor spheroids. First, the prepared FPNTs and cells (HCT-8 and NIH3T3 with a 1 : 1 ratio) were mixed and incubated for 9 days to form a multicellular spheroid. Furthermore, the tumors were collected, cleaned, stained, and sealed for imaging at 2, 5, and 9 days. The detailed temperature measurement setup and procedure are described in ESI section 1.9.†

### 2.10 Statistical analysis

For curve fitting processes, Origin software was used for analyzing the graphs. The data are presented as the means  $\pm$  standard error of the mean of at least three independent biological experiments. Statistical analyses on data containing more than two groups were performed using one-way ANOVA for multiple comparisons. Here,  $P < 0.05$  was considered statistically significant.

## 3. Results

### 3.1 Synthesis of fluorescent FPNTs

Rh-B dyes are fluorescent dyes that emit fluorescence intensity when exposed to light. These dyes were employed in producing various luminous functional particles, for example, polystyrene microspheres, polymeric microparticles, hydrogel-based particles, and silica particles.<sup>41,48,52,57,58</sup> Particularly, Rh-B dyes exhibit a unique temperature-based intensity-changing property and have been used as nano-thermometers.<sup>59</sup> On the other hand, Rh-B dyes are polar molecules that are highly soluble in water and other solvents. In particular, Rh-B is more actively diffused/leaks out from the polymerized materials than other dyes. For example, rhodamine-6G loaded microspheres show low leakage abilities than Rh-B from the same microspheres. On the other hand, covalent bonding between the dye and the matrix material may influence the temperature-based fluorescence intensity properties. Dyes grafted with polymeric particles exhibit reduced temperature sensitivity.<sup>60</sup> To overcome these problems, a method is necessary to solve the issues of leakage and lower sensitivity.<sup>59</sup> In this study, we followed a three-step procedure for the preparation of mono-

disperse temperature-sensitive FPNTs [Fig. 1]. The Rh-B dye was mixed with the amphiphilic copolymer Pluronic F-127 to form a dye-micelle complex (DMC) [Fig. 1(a)]. Furthermore, the DMC was processed and crosslinked with UPF resin. Usually, at neutral pH (pH 7), UPF resin forms methyl derivatives [Fig. 1(b)]. This DPMC was condensed under acidic conditions ( $\sim$ at pH 3), which leads to the formation of highly crosslinked 3D network (hydroxy methyl terminal group) particles [Fig. 1(c) and (d)]. Hence, Rh-B molecules were homogeneously incorporated into the polymer composite nanoparticles and covalently enclosed in the 3D cross-linked UPF resin with unchanged fluorescence properties. The detailed reaction mechanism is presented in ESI section 2.†

### 3.2 Morphology and size characterization of fluorescent FPNTs

The composition, charge, morphology, and size of the FPNTs were evaluated using FTIR,  $^1\text{H}$  NMR, DLS, and SEM. The FTIR spectroscopy results in Fig. 2(a) exhibit the composition of polymer complexes. The FTIR spectra of FPNTs (black color) show major distinct absorption bands of UPF resin, the peaks at  $1634\text{ cm}^{-1}$  and  $864\text{ cm}^{-1}$  represent the vibrations of the 1,3,5-s-triazine ring and the band at  $3341\text{ cm}^{-1}$  represents the vibration of the amino ( $-\text{NH}^-$ ) group. Furthermore, the bands at  $2893\text{ cm}^{-1}$  ( $-\text{CH}_2$  asymmetric stretching mode) and  $1343\text{ cm}^{-1}$  ( $-\text{CH}_2$  wagging vibration) are attributed to the presence of Pluronic F-127.<sup>61</sup> These results show that the FPNTs are formed with a blend of UPF and F-127 polymers. In particular, the absorption bands of Rh-B were not identified clearly in the obtained FTIR spectra. This may be because of the small concentration of Rh-B compared to the other blended polymers. However, the band at  $593.89\text{ cm}^{-1}$  is attributed to the primary alcohols, and the band at  $3367\text{ cm}^{-1}$  is attributed to the  $-\text{NH}_3$  stretching.<sup>62</sup> Also, some of the absorption peaks of the Rh-B dye were mixed with the absorption peaks of F-127 and UPF scaffolding polymers. FPNTs are a combination of three polymers (Pluronic F-127, urea, and paraformaldehyde). Furthermore, ESI Fig. S11† depicts the proton NMR ( $^1\text{H}$  NMR) spectra of FPNTs and offers information on the peaks produced for various chemical groups such as the appearance of amine groups [ $-\text{NHCH}_2\text{NH}_2$ ; 1.2 ppm] and primary amide hydrogen [ $-\text{NHCONH}_2$ ; 4.3 ppm]. Reacting urea and paraformaldehyde in an acidic medium ( $\sim$ pH 3) gives peaks at 2.4 ppm and 2.6 ppm, indicating the formation of methylene between secondary and/or tertiary amide hydrogens.<sup>63</sup> The prominent appearance of a peak at 3.4 ppm also shows clear evidence of the presence of methylol groups [ $-\text{NHCH}_2\text{OH}$ ; 3.4 ppm].<sup>63</sup> The diminished appearance of the peak at 4.6–5.0 ppm due to primary amide hydrogens also shows that the FPNT structure became more cross-linked due to the methylenization reaction.<sup>63</sup> Moreover, the presence of Rh-B dye clearly shows peaks at 1.0 ppm and 3.6 ppm due to the methyl group ( $-\text{CH}_3$ ) and a methylene group ( $-\text{CH}_2$ ) respectively.<sup>64</sup> Apart from that, peaks range from 7.0 to 7.4 ppm and 8.9 ppm represent hydrogen bonding ( $-\text{H}$ ).<sup>64</sup> The signals at 3.8 ppm and 3.3 ppm are related to the  $-\text{CH}_2\text{CH}_2\text{O}-$



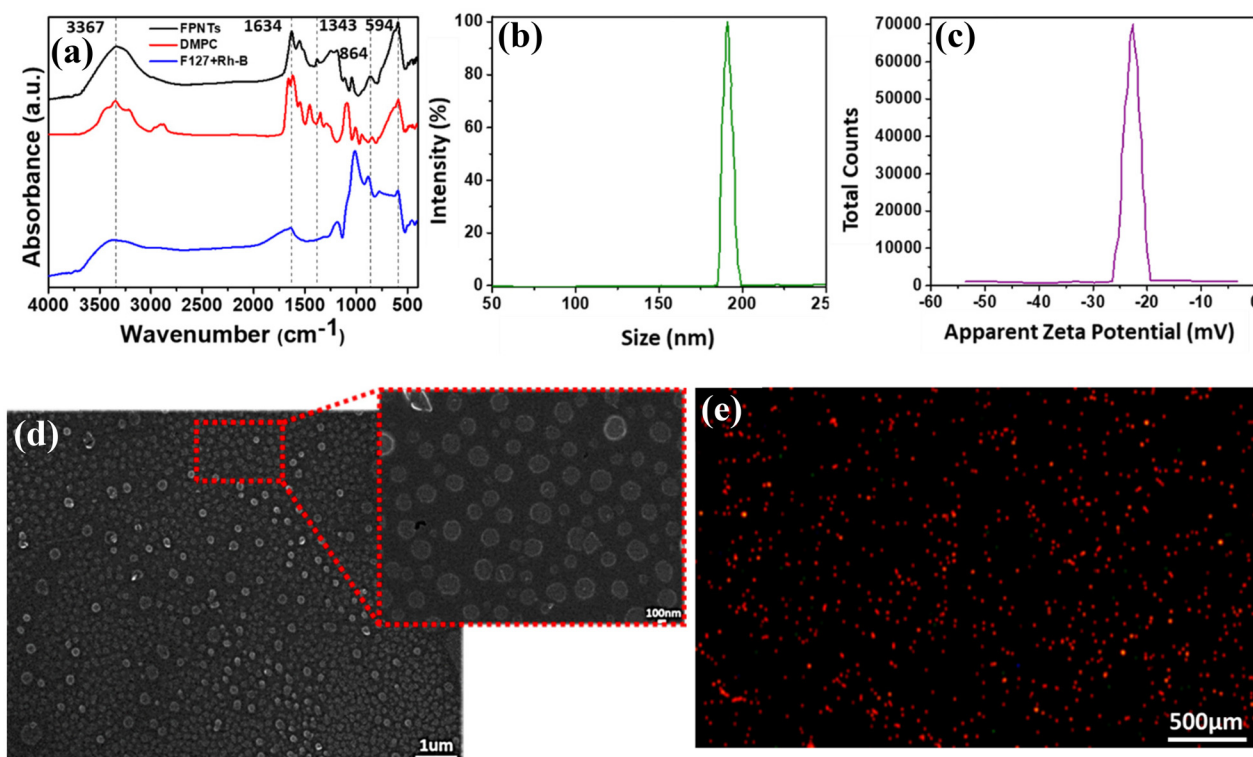


**Fig. 2** Structural and morphological characterization of FPNTs using the (a) FTIR spectra of the FPNTs, dye micelle polymer complex (DMPC), and F-127 + Rh-B dye. (b) Hydrodynamic diameter distribution and (c) zeta potential of FPNTs. (d) SEM image of FPNTs. (e) Fluorescence image of FPNTs.

and CH-O groups, respectively, which show the presence of Pluronic F-127.<sup>65</sup>

The DLS spectra provided access to the hydrodynamic particle sizes ( $Z_{avg}$ , nm) and size distribution. The results in Fig. 2(b) represent the monodispersed size distributions of FPNTs, with an average diameter of  $180 \pm 17$  nm. The zeta potential is a parameter characterizing the electrochemical equilibrium at the interfaces of electric structures. The properties of both the surface and the surrounding liquid play an important role in the theory of aggregative stability, also known as the Derjaguin, Landau, Verwey, and Overbeek (DLVO) theory.<sup>66</sup>

The zeta potential of the prepared FPNTs was  $-23$  mV [Fig. 2(c)]. The zeta potential of the nanoparticles with values  $>+25$  mV or  $<-25$  mV usually indicates a high degree of stability.<sup>67</sup> Lower dispersions of zeta potential values will lead to aggregation, coagulation, or flocculation due to van der Waals interparticle attraction. SEM was used to examine the morphology of the FPNTs that had been synthesized. It was found that the FPNTs obtained were extremely monodisperse spherical particles with an average diameter of  $166 \pm 10$  nm [Fig. 2(d)]. Overall, both DLS and SEM measurements showed a monodispersed size distribution of FPNTs with a small size difference. This difference may be because of the swelling nature of the particles in the colloidal solution.<sup>68</sup> The fundamental operating principle of FPNTs is based on the emission

of fluorescence light, which varies in intensity with temperature. The fluorescence image of FPNTs for further applications in temperature fluctuations in a small space is shown in Fig. 2(e).

### 3.3 Temperature and reversibility response of FPNT particles

The luminescence of Rh-B dye molecules can be influenced by temperature variation owing to the Boltzmann distribution of electrons within the excited state level.<sup>69</sup> The material's particular band structure vibration is a function of the temperature. As the temperature increases, thermal energy will excite the electrons in the excited state to multiple vibrational modes that overlap at different energy levels, hence nonradiative transitions will become feasible.<sup>69</sup> Fig. 3(b) shows the fluorescence spectra of the FPNTs in water as a function of temperature when excited at 553 nm and emitting at 627 nm, respectively. Due to the heating of the FPNTs particles, the encapsulated Rh-B dye undergoes a significant change in luminescence intensity, peak position, and bandwidth. This can be because higher temperatures will speed up the movement of the molecules (*i.e.*, higher translational energy), leading to collisions and more forceful collisions, thereby reducing the fluorescence intensity. The arrow depicts the progression of the maximum fluorescence emission wavelength, which is temperature-dependent as shown in Fig. 3(b). As the dye molecules are enclosed with the polymer and form nanoparticles, the fluo-

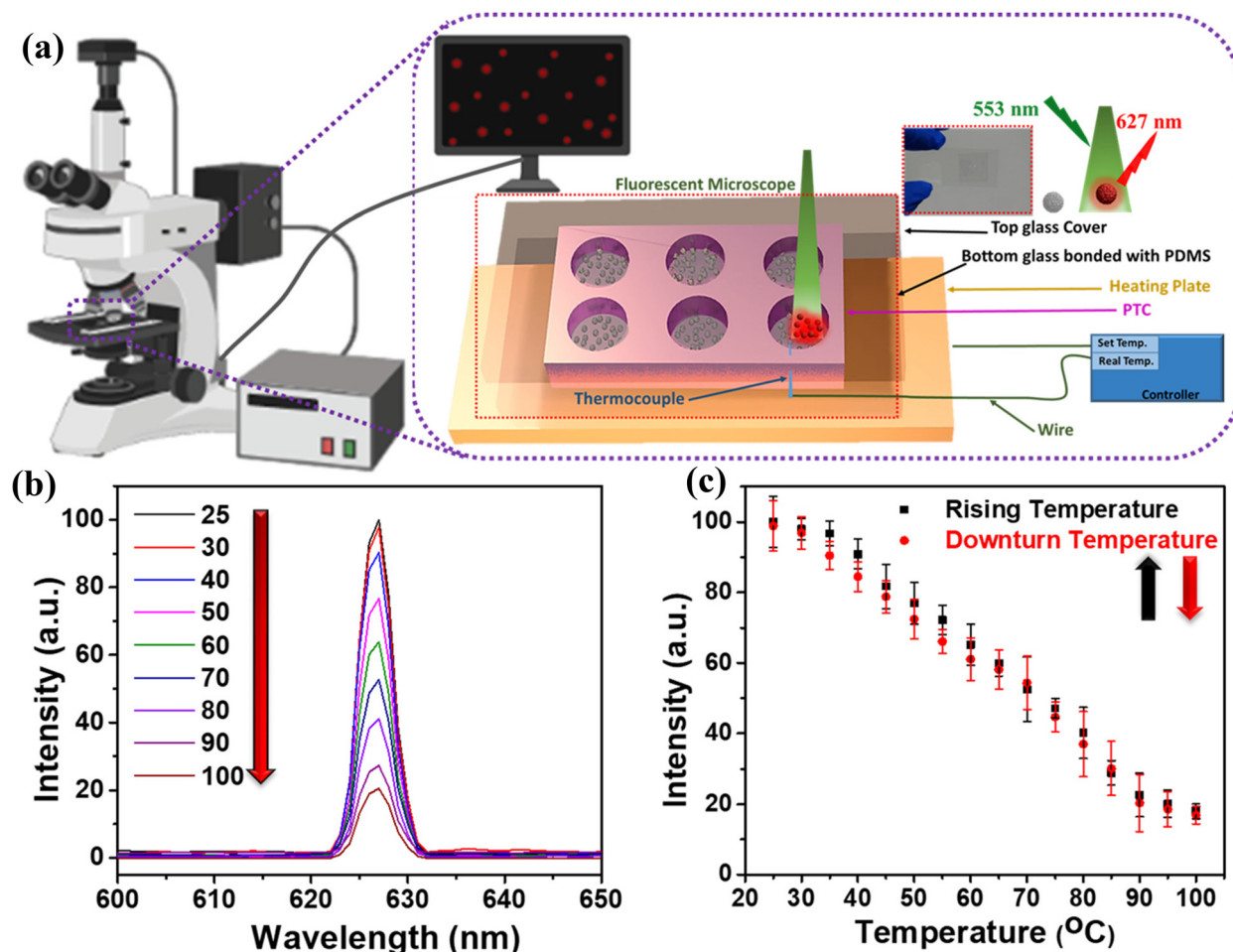


**Fig. 3** Temperature dependence of the fluorescence emission from the Rh-B encapsulated polymeric nanoparticles, FPNTs, dissolved in DI water. (a) Experimental set-up for the calibration of FPNTs. (b) Temperature-related emissions of the temperature-sensitive FPNTs using a fluorospectrometer dispersed in water in the temperature range of 25–100 °C. (c) Average fluorescence lifetime versus temperature during repeated heating and cooling and the corresponding linear regression.

rescence temperature responsiveness of Rh-B is significantly reduced.<sup>60</sup> The intensity of the FPNTs has a linear response to temperature changes over the range of 25–100 °C (at 5 °C intervals) as shown in Fig. 3(c). ESI Fig. S9 and S10† illustrate the correlation between the fluorescence intensity and temperature and the average fluorescence lifetime with temperature change, respectively. The reversibility of the thermometer was also examined by recording the fluorescence intensity of FPNTs from 100 to 25 °C (cooling process). The intensity decreases with temperature increase during the cooling process and shows a good linear relationship.

### 3.4 Dye leakage, stability, and quenching ability of FPNTs

For biomedical applications, the colloidal stability of fluorescent nanoparticles plays an important role. The dye release profile of the FPNTs was observed for 15 consecutive days. Initially, a burst effect was observed for the first 2 days, and 15–20% of Rh-B dye was released from the FPNT nanoparticles, and then a slow and sustained release was observed.

After 5–6 days, the releasing rate of the FPNTs was almost saturated, and it was observed that the emitted fluorescence intensity was from the properly encapsulated Rh-B dye (85–80%) as shown in Fig. 4(a). In addition, we investigated the quenching efficiency of the FPNTs with continuous and pulse exposure [ESI section 3† described in detail] of light for 50 minutes.

As depicted in Fig. 4(b), the intensity of FPNT fluorescence reduced slowly over the first 5 minutes (0.2–0.4%) and then reduces linearly for the next 25 minutes (between 5 and 30 minutes). After 35 minutes the fluorescence intensity of FPNTs decreased abruptly, which shows the stability of fluorescent light for a longer interval of time (~35 minutes). Also, we observed that the fluorescence intensity of FPNTs began to recover after 5 minutes. After 10 to 15 minutes, their intensity was retained by more than 60 percentage; and after 90 minutes, the FPNTs regained nearly their maximum intensity, demonstrating that the FPNTs have good reversibility and they could be used in multiple experiments. ESI Fig. S8† illustrates that the fluorescence intensity of FPNTs reduced slowly,

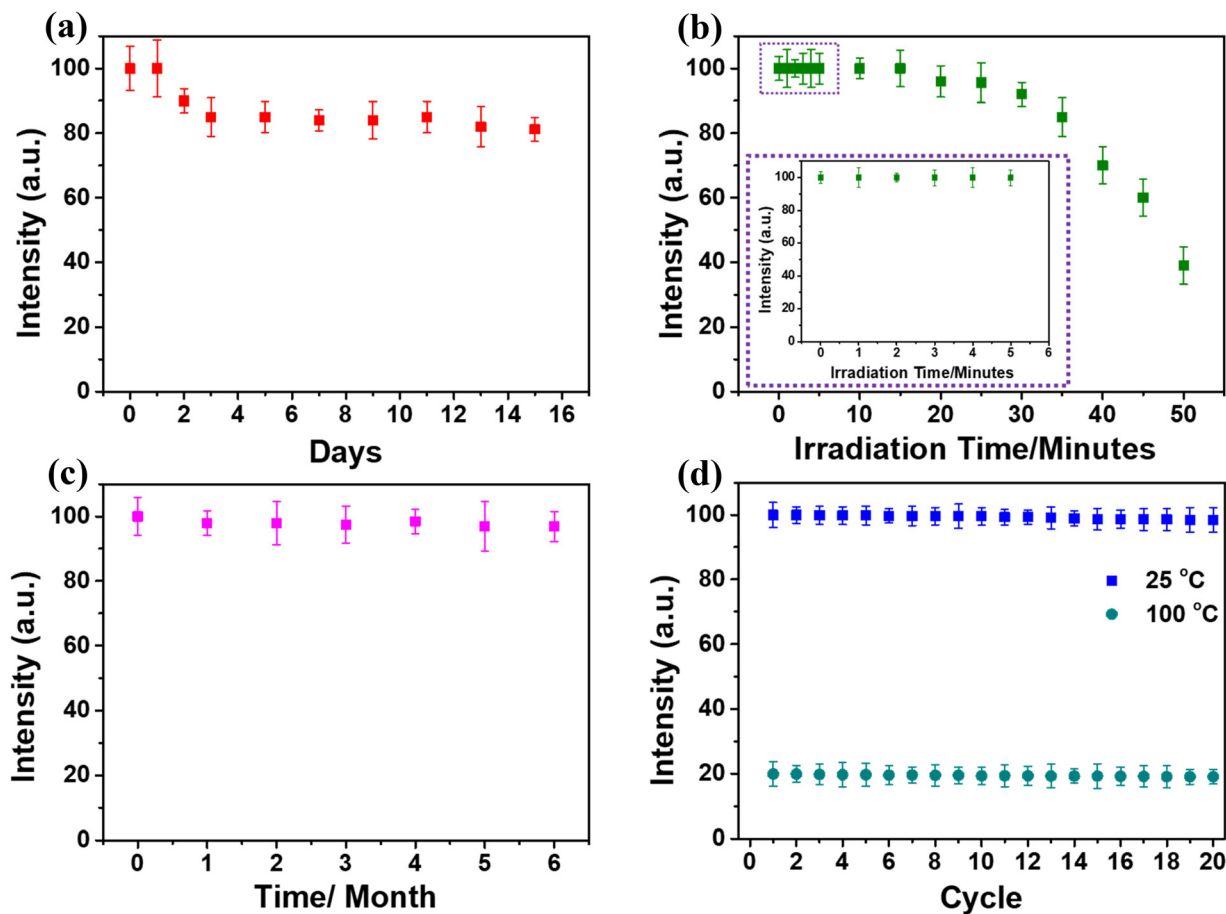


**Fig. 4** Performance assessment of FPNTs. (a) Dye leakage from the fabricated FPNTs. (b) Fluorescence lifetime of FPNTs as a function of irradiation time. (c) Fluorescence intensity of FPNTs vs. time. (d) Lifetime of FPNTs during repeated heating and cooling (cycling the temperature twenty times between 25 and 100 °C).

and ~6–7% change was observed for the first 5 cycles. Later, for the next 5 cycles (a total of 10 cycles), the intensity change was ~17% [the inset in ESI Fig. S8†], and finally, the intensity profile was changed linearly. Furthermore, the intensity stability of the FPNT particles for longer storage time and thermostability was tested as shown in Fig. 4(c) and (d), respectively. The results showed no intensity change in the FPNTs for ~6 months. However, the thermostability and temperature sensing ranges of the most reported fluorescent thermometers were restricted to 20–60 °C, particularly for fluorescence thermometers made of polymer materials.<sup>33,70</sup> To test the immediate heating and cooling stability, a total of twenty times repetitions of the FPNT solution were performed in the temperature range between 25 and 100 °C, as illustrated in Fig. 4(d). The figure shows that while the emission intensity of the sample changed with temperature, it maintained a high level of stability at the same temperature, demonstrating that the FPNTs had good thermostability.

### 3.5 pH, ion, and oxidative effect on FPNT particles

Various environmental factors affect nanoscale temperature imaging. These can be the pH, viscosity, and the presence of

different ions, and their strength can affect the accuracy of the fluorescent nanoparticles.<sup>55</sup> The biological nano/microenvironment is highly complex, and the environment varies with a variety of biological factors, such as pH, ionic strength, and viscosity, may affect the sensor's stability and accuracy. Thus, the temperature-sensing stability of the FPNTs in these harsh environments was investigated. An oxidative environment is generated when reactive oxygen species (ROS) are produced by a specific or by a combination of multiple stresses.<sup>71</sup> To investigate the stability of the FPNTs in an oxidative stress environment, 10 M H<sub>2</sub>O<sub>2</sub> has been diluted and prepared at different concentrations down to 1 nM. As shown in Fig. 5(a), the presence of H<sub>2</sub>O<sub>2</sub> does not affect the FPNT nanoparticles at low concentrations (1 nM–100 μM) but produces a minor variation at 500 μM. In an oxidative environment, the concentration increases beyond 500 μM, and the fluorescence intensity quenches sharply. The effect of ionic strength on the fluorescence intensity of FPNTs was also investigated. Fig. 5(b) shows that the fluorescence intensity of the FPNTs does not change even in different ionic solutions (KCl, NaOH, and NaCl) with a concentration of 2.0 mol L<sup>-1</sup> (at room temperature). We also studied the effect of pH on the fluorescence of FPNTs.

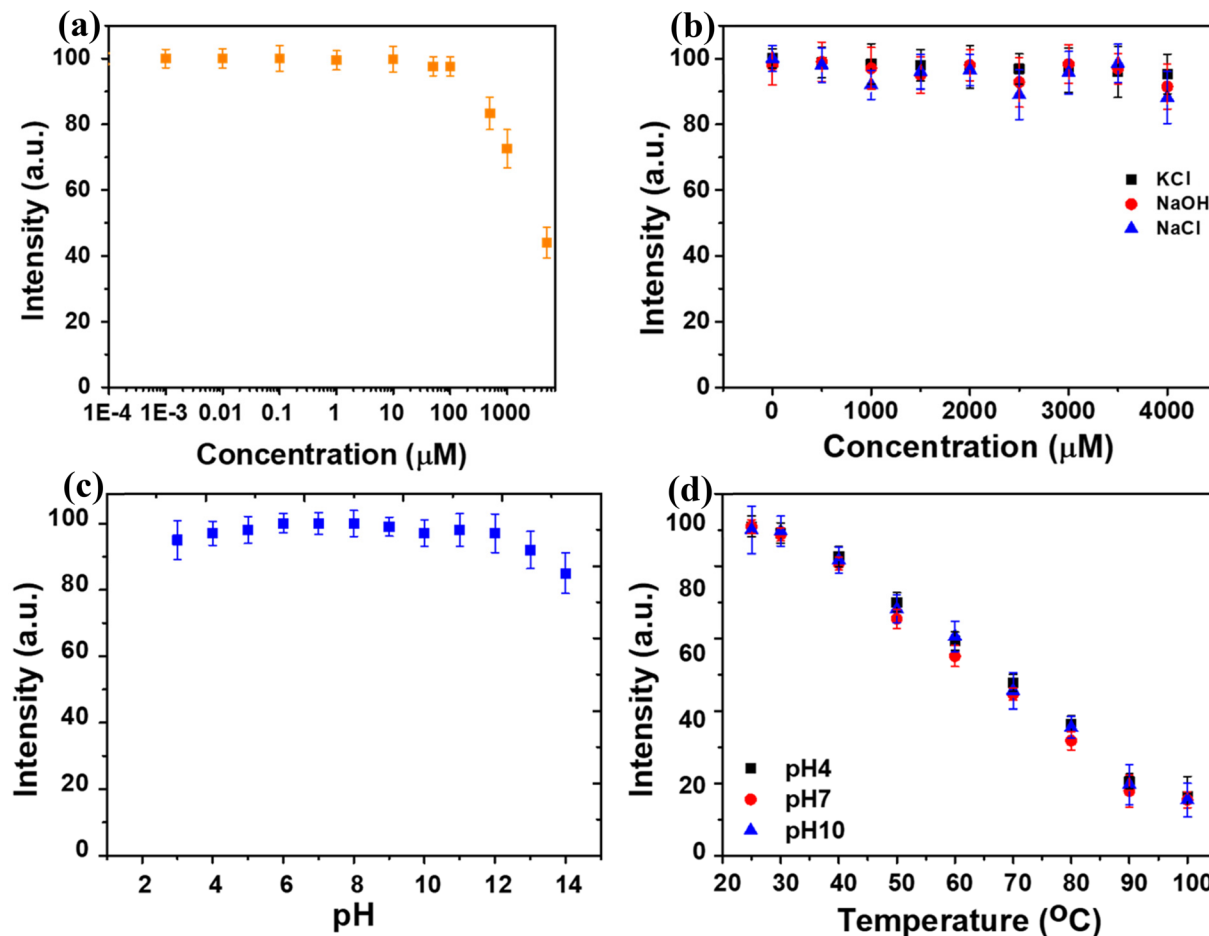


**Fig. 5** The environmental behavior of FPNTs. (a) Fluorescence intensity of FPNTs in  $\text{H}_2\text{O}_2$  solution with different concentrations. (b) Fluorescence intensity of FPNTs in KCl, NaOH, and NaCl solutions with different concentrations at room temperature. (c) Fluorescence intensity of FPNTs at various pH values. (d) Temperature sensing properties of FPNTs in solutions at various pH values.

As shown in Fig. 5(c), the fluorescence intensity remains unchanged over a pH range from 1 to 11. However, at higher pH ( $\text{pH} > 11.0$ ), the fluorescence intensity decreases sharply. The influences of different pH values on the temperature-sensing properties of FPNTs were investigated. Furthermore, pH 4, 7, and 10 were used to measure the sensing capabilities of the FPNTs. As shown in Fig. 5(d), the intensity was unchanged using three different pH values at different temperatures. These results show that the prepared FPNTs exhibit high sensing stability in various harsh environments, as can be explained by the isolation effect of the highly cross-linked UPF encapsulation matrix on the incorporated dyes.

### 3.6 3D distribution and dynamic monitoring of temperature in co-cultured 3D tumor spheroids

HCT-8 and NIH3T3 cells were co-cultured in a  $\mu$ -well 3D cell-culture platform as mentioned in our previous manuscript.<sup>56</sup> These two types of cells are self-organized into core-shell structures, HCT-8 cells localized into the center, and NIH3T3 confined to the shell (see ESI Fig. S5(b)†).

In our previous study, the live/dead assay showed 98.8% viability during the entire culture period.<sup>56</sup> As explained previously, 9 days old 3D *in vitro* spheroids exhibit complex desmoplastic reactions and hypoxic cores.<sup>56</sup> Hypoxia hinders many aspects of the cellular and systemic physiology of cancer cells, and the cells enter into a dormant state.<sup>72</sup> This hijacked cellular metabolism slightly reduces the heat production in that local area. The FPNTs in Fig. 6(e) represent the temperature distribution in 3D co-cultured spheroids at the exterior, interior, and core parts. The measured values represent the temperature variations from the exterior and interior regions to the core region as 37.8, 35.9, and 34.9  $^\circ\text{C}$ , respectively, which is consistent with the previous studies.<sup>73</sup>

## 4. Discussion

Temperature is rarely considered a critical entity in cancer biology. However, thermoregulation is an important factor that stimulates pro-cancer pathways and tumor microenvironment activities. Recent studies showed that cooler temperatures par-



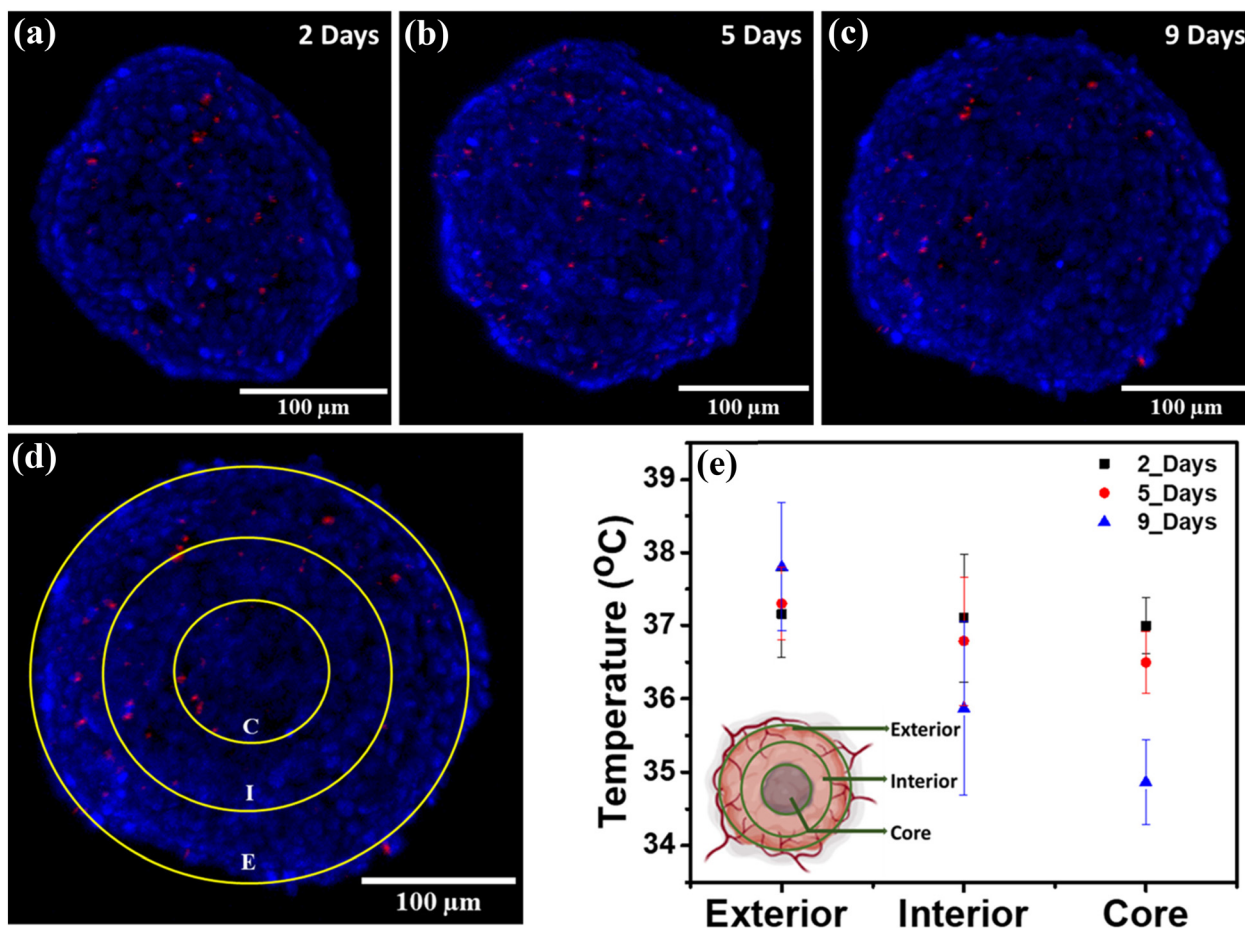


**Fig. 6** 3D-temperature distribution and dynamic monitoring of co-cultured tumor spheroids. (a–c) Confocal images representing 3D co-cultured tumor spheroids treated with FPNTs after 2, 5, and 9 days, respectively. (d) Spheroids treated with FPNTs, and the fluorescence intensity was measured at the center region (C), interior region (I), and exterior region (E). The center region showed a significantly higher fluorescence intensity compared to the exterior and interior regions. (e) Temperature distribution at different positions inside the spheroid after 9 days.

ticularly stimulate the activation of stress hormones like nor-epinephrine (NE).<sup>74</sup> In this direction, the overactivation of NE can proactively impact the cancer progression and metastasis in various cancer types.<sup>2–5</sup> Thus, providing a quick and non-invasive technique to measure the temperature is of paramount interest. In this context, a variety of nanosensors such as semiconductor quantum dots,<sup>13,23–26</sup> rare earth metal doped nanoparticles,<sup>22,23,27</sup> carbon dots,<sup>28–30</sup> and metal nanoclusters (MNCs)<sup>4,31–33</sup> with different techniques were developed to measure the temperature including at an intracellular level. However, the reported sensors remain limited by the temperature sensing range, toxicity, and thermostability of the fabricated materials as shown in Table 1. CdSe QDs,<sup>75</sup> CdSeS/ZnS@polymer sensor,<sup>76</sup> nanodiamonds (N-vacancy centers),<sup>77</sup> Au/Pd thermocouple,<sup>65</sup> and gTEMP fluorescent protein<sup>78</sup> sensors have maximum temperature sensing ranges of 25–45 °C, 30–60 °C, 54 °C, 17–37 °C, and 5–50 °C respectively. CdSe QDs exhibit a superior sensitivity of 0.015% °C<sup>–1</sup> but have limitations due to their narrow temperature sensing range (30–60 °C). However, the quantum dots show extraordinary quantum efficiency and are considered good candidates for

bio-imaging applications, but toxicity is a big concern, particularly for *in vivo* studies. The nano-gels that have been created using green fluorescent protein (GFP) sensors can only measure temperature within 15 °C of the gel's transition temperature.<sup>35</sup> The sensors constructed with silicon nanoparticles can detect temperatures ranging from 0 to 60 °C.<sup>36</sup> Though some of the sensors fabricated with inorganic materials showed a wider range of temperature sensing, they require ultraviolet (UV) light to read the results.<sup>79–81</sup> Thus, these issues limit their usage in biological applications. However, ratiometric sensors give accurate measurements but the setup and operation are more complex.<sup>82,83</sup> Hence, particularly sensors with a wide range of sensitivity, high resolution, biocompatibility and good thermostability are of significant interest in the biomedical industry.<sup>79–81</sup> In this study, we developed FPNTs by the sol-gel method, where the Rh-B dye incorporated Pluronic F-127 micelles were polymerized with a polymer complex (urea and paraformaldehyde) as shown in Fig. 1. In this 3-step process, Pluronic F-127 helped not only in the formation of UPF nanoparticles but also cross-linked with the Rh-B dye to form a dye-micelle polymer complex (DMPC).

**Table 1** Comparison of performance characteristics of the temperature sensors

Type of sensor	Temperature range (°C)	Sensitivity	Reversibility	Calibration environment	Cell types	Cellular level	Ref.
CdSeS/ZnS@polymer	25–45	$-1.55\% \text{ } ^\circ\text{C}^{-1}$	Positive	In water	HepG2	Dotted inside the cell	77
CdSe QDs	30–60	$0.015\% \text{ } ^\circ\text{C}^{-1}$	Positive	In PBS	Mouse tissue	Local tissue	68
Nano needle	24–60	N/A	Positive	In water	N/A	The local region in the cell	69
Au nanoclusters	15–45	N/A	Positive	In cell	HeLa	Dotted in the cell	27
Nanodiamonds (N-vacancy centers)	54	N/A	Positive	In air	WS1	Dotted in the cell	70
Au/Pd thermocouple	17–37	N/A	N/A	In cell	N/A	Subcellular	78
Si resonator	30–59	$-1900 \text{ ppm } \text{K}^{-1}$	N/A	In cell	N/A	Single-cell	79
gTEMP fluorescent protein	5–50	N/A	Positive	In cell	HeLa	Subcellular	71
FPNTs	25–100	$1.1 \text{ } ^\circ\text{C}$	Positive	In glycerol	3D co-Culture	HCT-8 and NIH3T3	Present work

Pluronic F-127 is an amphiphilic co-polymer and its hydrophilic ends and hydrophobic center parts can be used for molecular functionalization and for cross-linking to form a micelle. Moreover, F-127 has been widely used in biological applications because of its stability, constructive mechanical properties, biocompatibility, and low toxicity.<sup>84</sup> On the other hand, urea-formaldehyde (UPF), which is an amino resin with a strongly cross-linked internal structure that exhibits high thermostability and interior space to load fluorescent particles and dye-micelles by comparing it to other polymer complexes.<sup>49,85</sup> As a result, the DMC could be strongly cross-linked in UPF in the prepared FPNTs with lower leakage.<sup>51</sup> Apart from that, F-127 and UPF matrices produce biocompatible nanoparticles, which are useful for *in vitro* and *in vivo* experiments. Because of these superlative properties F-127 and UPF were selected in this study to form highly cross-linked FPNTs. The fabricated FPNTs were designed such that they can maintain the chemical stability or functionality of fluorescent dye and prevent interference from strong oxidation conditions as shown in Fig. 5(a–d), and they can endure severe treatments, such as high-temperature sterilization (100 °C) [Fig. 3(c)] and low-temperature preservation (–20 °C) [Fig. 4(c)]. The results demonstrate that FPNTs are monodispersed, have excellent fluorescence intensity, and exhibit a temperature range between 25 and 100 °C with a resolution of 1.1 °C. Moreover, the prepared FPNTs show good biocompatibility and encapsulation effectiveness (80–85%) [Fig. 4(a)], and prevent interference from strong oxidation conditions inside the tumor microenvironment (TME). In the TME reactive oxygen species (ROS) molecules are produced in higher concentrations and these ROS molecules may involve in quenching the fluorescence of nanoparticles (FPNTs) but our results in Fig. 5(a–d) show that the FPNTs are stable under different environmental conditions and the fluorescence intensity was stable [Fig. 4(b)] until 5 min with continuous exposure to light.

As a result, the Rh-B dye micelle molecules could be tightly bound in the synthesized nanoparticles. The temperature sensor exhibits a temperature-dependent changing emission property, which can sense temperatures ranging from 25 to 100 °C without agglomeration and dye leakage. Moreover, the FPNTs exhibit better stability against different environmental

factors such as pH, ionic strength, and oxidative stress as shown in Fig. 5(a–d). Further, the FPNTs show good biocompatibility (see ESI Fig. S4†). These properties make them suitable for measuring the temperature at the cellular level and even in 3D spheroids. More importantly, we incorporated these sensors with 3D co-cultured tumor spheroids to measure the temperature gradient. Particularly, the hypoxic condition reduces the activation of thermogenic mechanisms, thus, the condition reduces the body temperature in mammals by 8–10 °C.<sup>86</sup> Hypoxia suppresses the anti-tumor activity and vascularization in cancer tumors, and induces a pro-active cancer tumor microenvironment. The 3D co-cultured tumor model orchestrates an *in vivo*-like cellular arrangement and exhibits a desmoplastic environment to induce hypoxia and epithelial-mesenchymal transition (EMT) as presented in the previous work.<sup>56</sup> These cascades of events in the 3D tumor spheroids may cause a lower temperature in the core region, and the measured temperature in the co-cultured tumor spheroids showed a  $\sim 2.9 \text{ } ^\circ\text{C}$  difference from the core region to the peripheral region. This provides strong support for the hypothesis that a reduction in the activation of thermogenic mechanisms in the hypoxia region occurred. The present observations open up several intriguing possibilities. For instance, real-time and dynamic measurement at the cellular level temperature gradient could enable an accurate understanding of cellular activity and cancer progression.

## 5. Conclusions

In this study, we developed novel FPNTs and measured temperature gradients in co-cultured 3D tumor spheroids. The novel FPNTs were designed and fabricated by embedding temperature-sensitive Rh-B dye inside polymeric nanoparticles to maintain its chemical stability or functionality, reduce cell toxicity, and prevent interference from strong oxidation conditions inside the TME. The results demonstrate that the FPNTs are monodisperse, have excellent fluorescence intensity, and exhibit a temperature range between 25 and 100 °C, with a resolution of 1.1 °C. The FPNT nanoparticles had an encapsulation effectiveness of 80–85%, and only 15–20% dye was released. Individual FPNTs are internalized inside the co-cul-

tured spheroids to dynamically measure the temperature changes in the 3D spheroids from the core region to the peripheral region at different time intervals. It was observed that the temperature in an exterior section of the spheroid was high compared to that at the center. This can be due to a lack of sufficient oxygen in the environment, which results in anaerobic respiration. All of these results showed that FPNTs could be suitable candidates to explore hyperthermia processes in tumor microenvironments as nano-thermometers and it is expected that they contribute to the examination of various biological events in the near future.

## Abbreviations

FPNTs	Fluorescent polymeric nano-thermometers
DMPC	Dye micelle polymer complex
UPF	Urea paraformaldehyde
3D	Three-dimensional
2D	Two-dimensional
μ-well	Three-dimensional microwell cell-culture array
3D	platform
TME	Tumor micro environment
PDMS	Polydimethylsiloxane
IC <sub>50</sub>	Inhibitory concentration
SEM	Scanning electron microscopy
DLS	Dynamic light scattering
ROS	Reactive oxygen species

## Conflicts of interest

The authors agree to be responsible for all aspects of the work and have no competing financial interests.

## Acknowledgements

We would like to thank the financial support from the Ministry of Science and Technology (MOST), Taiwan (MOST110-2731-M-007-001 and MOST110-2221-E-007-017-MY3), the Frontier Research Center on Fundamental and Applied Sciences of Matters, the Featured Areas Research Center Program within the framework of the Higher Education Sprout Project by the Ministry of Education (MOST 111-2634-F-007-007 and MOE111QR001I5), the Veterans General Hospital and University System of the Taiwan Joint Research Program (VGHUST) (VGHUST109-V6-1-1 and VGHUST111-G5-1-1), the National Health Research Institutes (NHRI-EX111-11126BI) and the DBT/Wellcome Trust India Alliance Fellowship (IA/E/16/1/503062).

## References

- 1 J. Lee Kavanau, *J. Gen. Physiol.*, 1950, **34**(2), 193–209.
- 2 N. Inada and S. Uchiyama, *Imaging Med.*, 2013, **5**, 303–305.
- 3 M. Monti, L. Brandt, J. Ikomi-Kumm and H. Olsson, *Scand. J. Haematol.*, 1986, **36**, 353–357.
- 4 P. Yu, X. Wen, Y. R. Toh and J. Tang, *J. Phys. Chem. C*, 2012, **116**, 25552–25557.
- 5 L. Kavanau, *J. Gen. Physiol.*, 1950, **34**(2), 193–209, DOI: [10.1085/jgp.34.2.193](https://doi.org/10.1085/jgp.34.2.193).
- 6 J. W. L. Eng, C. B. Reed, K. M. Kokolus, R. Pitoniak, A. Utley, M. J. Bucsek, W. W. Ma, E. A. Repasky and B. L. Hylander, *Nat. Commun.*, 2015, **6**, DOI: [10.1038/NCOMMS7426](https://doi.org/10.1038/NCOMMS7426).
- 7 K. E. Conley and W. P. Porter, *J. Exp. Biol.*, 1986, **126**, 249–269.
- 8 B. Cannon and J. Nedergaard, *J. Exp. Biol.*, 2011, **214**, 242–253.
- 9 M. Suzuki and T. Plakhotnik, *Biophys. Rev.*, 2020, **12**, 593–600.
- 10 F. Yang, G. Li, J. Yang, Z. Wang, D. Han, F. Zheng and S. Xu, *Sci. Rep.*, 2017, **7**, 1–12.
- 11 K. Krumova, G. Cosa, J. Aubry and J. R. Kanofsky, *Singlet Oxyg. Appl. Biosci. Nanosci.*, 2016, 1–4.
- 12 J. Feng, L. Xiong, S. Wang, S. Li, Y. Li and G. Yang, *Adv. Funct. Mater.*, 2013, **23**, 340–345.
- 13 A. N. Generalova, V. A. Oleinikov, A. Sukhanova, M. V. Artemyev, V. P. Zubov and I. Nabiev, *Biosens. Bioelectron.*, 2013, **39**, 187–193.
- 14 C. Wang, T. Hu, T. Thomas, S. Song, Z. Wen, C. Wang, Q. Song and M. Yang, *Nanoscale*, 2018, **10**, 21809–21817.
- 15 K. Xue, C. Wang, J. Wang, S. Lv, B. Hao, C. Zhu and B. Z. Tang, *J. Am. Chem. Soc.*, 2021, **143**, 14147–14157.
- 16 L. Li, F. Qin and Z. Zhang, *CrystEngComm*, 2019, **21**, 3256–3263.
- 17 C. Rennero-Lecuna, A. Herrero, D. Jimenez De Aberasturi, M. Martínez-Flórez, R. Valiente, M. Mychinko, S. Bals and L. M. Liz-Marzán, *J. Phys. Chem. C*, 2021, **25**(36), 19887–19896, DOI: [10.1021/acs.jpcc.1c05828](https://doi.org/10.1021/acs.jpcc.1c05828).
- 18 L. Shi, X. Dong, G. Zhang, Y. Zhang, C. Zhang, C. Dong and S. Shuang, *Anal. Methods*, 2021, **13**, 3561–3568.
- 19 D. Stefańska, B. Bondzior, T. H. Q. Vu, N. Miniajluk-Gawel and P. J. Dereń, *J. Alloys Compd.*, 2020, **842**, 3–12.
- 20 Y. Yang, W. Kong, H. Li, J. Liu, M. Yang, H. Huang, Y. Liu, Z. Wang, Z. Wang, T. K. Sham, J. Zhong, C. Wang, Z. Liu, S. T. Lee and Z. Kang, *ACS Appl. Mater. Interfaces*, 2015, **7**, 27324–27330.
- 21 J. Xue, M. Song, H. M. Noh, S. H. Park, B. C. Choi, J. H. Kim, J. H. Jeong and P. Du, *J. Alloys Compd.*, 2020, **843**, 155858.
- 22 A. Maruyama, Y. Matsumoto and H. Nakagawa, *Agric. For. Meteorol.*, 2020, **292–293**, 108028.
- 23 X. Guan, L. Wang, M. Liu, K. Wang, X. Yang, Y. Ding, J. Tong, Z. Lei and S. Lai, *Mater. Chem. Front.*, 2021, **5**, 355–367.
- 24 T. Kavitha, J. O. Kim, S. Jang, D. P. Kim, I. K. Kang and S. Y. Park, *Mater. Sci. Eng., C*, 2016, **61**, 492–498.
- 25 P. Zuo, J. Liu, H. Guo, C. Wang, H. Liu, Z. Zhang and Q. Liu, *Anal. Bioanal. Chem.*, 2019, **411**, 1647–1657.
- 26 C. D. S. Brites, P. P. Lima, N. J. O. Silva, A. Millán, V. S. Amaral, F. Palacio and L. D. Carlos, *Nanoscale*, 2012, **4**, 4799–4829.

- 27 R. Sakaguchi, S. Kiyonaka and Y. Mori, *Curr. Opin. Biotechnol.*, 2015, **31**, 57–64.
- 28 L. Shang, F. Stockmar, N. Azadfar and G. U. Nienhaus, *Angew. Chem., Int. Ed.*, 2013, **52**, 11154–11157.
- 29 S. Uchiyama, Y. Matsumura, A. P. De Silva and K. Iwai, *Anal. Chem.*, 2004, **76**, 1793–1798.
- 30 M. Suzuki, V. Tseeb, K. Oyama and S. Ishiwata, *Biophys. J.*, 2007, **92**, L46–L48.
- 31 J. M. Yang, H. Yang and L. Lin, *ACS Nano*, 2011, **5**, 5067–5071.
- 32 M. Nakano and T. Nagai, *J. Photochem. Photobiol., C*, 2017, **30**, 2–9.
- 33 T. Hayashi, N. Fukuda, S. Uchiyama and N. Inada, *PLoS One*, 2015, **10**, 1–18.
- 34 H. Gao, C. Kam, T. Y. Chou, M. Y. Wu, X. Zhao and S. Chen, *Nanoscale Horiz.*, 2020, **5**, 488–494.
- 35 J. Qiao, Y. H. Hwang, C. F. Chen, L. Qi, P. Dong, X. Y. Mu and D. P. Kim, *Anal. Chem.*, 2015, **87**, 10535–10541.
- 36 G. Al-Chaar, T. Hoang, D. Dowds, K. Ford, T. Carlson and C. Marsh, *J. Cluster Sci.*, 2014, **25**, 559–570.
- 37 M. N. Getz, O. Nilsen and P. A. Hansen, *Sci. Rep.*, 2019, **9**, 1–11.
- 38 S. Liang, S. Liang, Y. Wang, Y. Wang, L. Mu, G. She, W. Shi and W. Shi, *Nanotechnology*, 2020, **31**, DOI: [10.1088/1361-6528/ab95b6](https://doi.org/10.1088/1361-6528/ab95b6).
- 39 F. Hou, B. Xi, X. Wang, Y. Yang, H. Zhao, W. Li, J. Qin and Y. He, *Colloids Surf., B*, 2019, **183**, 110441.
- 40 V. M. Chauhan, R. H. Hopper, S. Z. Ali, E. M. King, F. Udrea, C. H. Oxley and J. W. Aylott, *Sens. Actuators, B*, 2014, **192**, 126–133.
- 41 C. Roth. Safety, *Data Sheet Rhodamine B (C.I. 45170) for Microscopy*, 2019, **0**, 1–11.
- 42 L. M. Skjolding, L. v, G. Jørgensen, K. S. Dyhr, C. J. Köppl, U. S. McKnight, P. Bauer-Gottwein, P. Mayer, P. L. Bjerg and A. Baun, *Water Res.*, 2021, **197**, 117109.
- 43 T. Nguyen and M. B. Francis, *Org. Lett.*, 2003, **5**, 3245–3248.
- 44 A. Cano, E. Sánchez-López, M. Ettcheto, A. López-Machado, M. Espina, E. B. Souto, R. Galindo, A. Camins, M. L. García and P. Turowski, *Nanomedicine*, 2020, **15**, 1239–1261.
- 45 M. T. Chevalier, J. Gonzalez and V. Alvarez, *IFMBE Proc.*, 2015, **49**, 187–190.
- 46 A. Cano, M. Ettcheto, J. H. Chang, E. Barroso, M. Espina, B. A. Kühne, M. Barenys, C. Auladell, J. Folch, E. B. Souto, A. Camins, P. Turowski and M. L. García, *J. Controlled Release*, 2019, **301**, 62–75.
- 47 C. C. Hopkins and J. R. de Bruyn, *J. Rheol.*, 2019, **63**, 191–201.
- 48 S. Chatterjee, P. C. leung Hui, C. wai Kan and W. Wang, *Sci. Rep.*, 2019, **9**, 1–13.
- 49 Y. Wu, Y. Li, J. Xu and D. Wu, *J. Mater. Chem. B*, 2014, **2**, 5837–5846.
- 50 J. Li and Y. Zhang, *Polymer*, 2021, **13**, 1–17.
- 51 C. Gonçalves, J. Pereira, N. Paiva, J. Ferra, J. Martins, F. Magalhaes, A. Barros-Timmons and L. Carvalho, *Ind. Eng. Chem. Res.*, 2019, **58**, 5665–5676.
- 52 Z. Yang, H. Peng, W. Wang and T. Liu, *J. Appl. Polym. Sci.*, 2010, **116**, 2658–2667.
- 53 D. Bokov, A. Turki Jalil, S. Chupradit, W. Suksatan, M. Javed Ansari, I. H. Shewael, G. H. Valiev and E. Kianfar, *Adv. Mater. Sci. Eng.*, 2021, **2021**, 1–21, DOI: [10.1155/2021/5102014](https://doi.org/10.1155/2021/5102014).
- 54 Y. Liu, S. Fu, L. Lin, Y. Cao, X. Xie, H. Yu, M. Chen and H. Li, *Int. J. Nanomed.*, 2017, **12**, 2635–2644.
- 55 G. A. Ormondroyd, *Adhesives for wood composites*, Elsevier Ltd, 2015.
- 56 V. S. Goudar, M. P. Koduri, Y. N. N. Ta, Y. Chen, L. A. Chu, L. S. Lu and F. G. Tseng, *ACS Appl. Mater. Interfaces*, 2021, **13**, 48478–48491.
- 57 M. A. Ali, J. Moghaddasi and S. A. Ahmed, *Laser Chem.*, 1991, **11**, 31–38.
- 58 N. Nishiyama, T. Zheng, Y. Yamane, Y. Egashira and K. Ueyama, *Carbon*, 2005, **43**, 269–274.
- 59 Z. Zhang, Y. Long, J. Pan and X. Yan, *J. Mater. Chem.*, 2010, **20**, 1179–1185.
- 60 F. Ye, C. Wu, Y. Jin, Y. H. Chan, X. Zhang and D. T. Chiu, *J. Am. Chem. Soc.*, 2011, **133**, 8146–8149.
- 61 Y. Liu, S. Fu, L. Lin, Y. Cao, X. Xie, H. Yu, M. Chen and H. Li, *Int J Nanomedicine*, 2017, **12**, 2635–2644, DOI: [10.2147/IJN.S122746](https://doi.org/10.2147/IJN.S122746).
- 62 R. Singh, O. P. Ahlawat and A. Rajor, *Bull. Environ., Pharmacol. Life Sci.*, 2017, **6**, 53–66.
- 63 M. O. Edoga, *Bull. Environ., Pharmacol. Life Sci.*, 2006, 63–80.
- 64 W. Li, W. Wang, Y. Yang and K. Zhang, *J. Mater. Chem. A*, 2014, **2**, 13675–13681.
- 65 M. Shaikhullina, A. Khaliullina, R. Gimatdinov, A. Butakov, V. Chernov and A. Filippov, *J. Mol. Liq.*, 2020, **306**, DOI: [10.1016/j.molliq.2020.112898](https://doi.org/10.1016/j.molliq.2020.112898).
- 66 F. Gabor, *Sci. Pharm.*, 2011, **79**, 701–702.
- 67 A. J. Shnoudeh, I. Hamad, R. W. Abdo, L. Qadumii, A. Y. Jaber, H. S. Surchi and S. Z. Alkelany, *Synthesis, Characterization, and Applications of Metal Nanoparticles*, Elsevier Inc., 2019.
- 68 E. Drioli and L. Giorno, *Encyclopedia of Membranes*, 2016, DOI: [10.1007/978-3-662-44324-8](https://doi.org/10.1007/978-3-662-44324-8).
- 69 X. D. Wang, O. S. Wolfbeis and R. J. Meier, *Chem. Soc. Rev.*, 2013, **42**, 7834–7869.
- 70 K. Okabe, N. Inada, C. Gota, Y. Harada, T. Funatsu and S. Uchiyama, *Nat. Commun.*, 2012, **3**, 705, DOI: [10.1038/ncomms1714](https://doi.org/10.1038/ncomms1714).
- 71 G. W. Thorpe, C. S. Fong, N. Alic, V. J. Higgins and I. W. Dawes, *Proc. Natl. Acad. Sci. U. S. A.*, 2004, **101**, 6564–6569.
- 72 G. L. Semenza, *Am. J. Physiol.: Cell Physiol.*, 2011, **301**, 550–552.
- 73 K. Otsuka, Y. Yamamoto and T. Ochiya, *J. Extracell. Vesicles*, 2020, **10**(2), DOI: [10.1002/jev2.12049](https://doi.org/10.1002/jev2.12049).
- 74 D. Palm, K. Lang, B. Niggemann, T. L. Drell IV, K. Masur, K. S. Zaenker and F. Entschladen, *Int. J. Cancer*, 2006, **118**, 2744–2749.
- 75 L. M. Maestro, P. Haro-González, B. Del Rosal, J. Ramiro, A. J. Caamaño, E. Carrasco, A. Juarranz, F. Sanz-Rodríguez, J. G. Solé and D. Jaque, *Nanoscale*, 2013, **5**, 7882–7889.



- 76 M. F. A. Muhammad Rashidi Wahab, *J. Teknol.*, 2013, **3**, 31–39.
- 77 G. Kucsco, P. C. Maurer, N. Y. Yao, M. Kubo, H. J. Noh, P. K. Lo, H. Park and M. D. Lukin, *Nature*, 2013, **500**, 54–58.
- 78 M. Nakano, Y. Arai, I. Kotera, K. Okabe, Y. Kamei and T. Nagai, *PLoS One*, 2017, **12**, 1–14.
- 79 A. Cadiau, C. D. S. Brites, P. M. F. J. Costa, R. A. S. Ferreira, J. Rocha and L. D. Carlos, *ACS Nano*, 2013, **7**, 7213–7218.
- 80 S. Zheng, W. Chen, D. Tan, J. Zhou, Q. Guo, W. Jiang, C. Xu, X. Liu and J. Qiu, *Nanoscale*, 2014, **6**, 5675–5679.
- 81 X. Rao, T. Song, J. Gao, Y. Cui, Y. Yang, C. Wu, B. Chen and G. Qian, *J. Am. Chem. Soc.*, 2013, **135**, 15559–15564.
- 82 T. Zhao, K. Asawa, T. Masuda, A. Honda, K. Kushiro, H. Cabral and M. Takai, *J. Colloid Interface Sci.*, 2021, **601**, 825–832.
- 83 A. Bigdeli, F. Ghasemi, S. Abbasi-Moayed, M. Shahrajabian, N. Fahimi-Kashani, S. Jafarinejad, M. A. Farahmand Nejad and M. R. Hormozi-Nezhad, *Anal. Chim. Acta*, 2019, **1079**, 30–58.
- 84 A. P. Constantinou and T. K. Georgiou, *Polym. Int.*, 2021, **70**, 1433–1448.
- 85 Y. Li, Y. Wu, C. Luo, B. Wang and D. Wu, *J. Mater. Chem. C*, 2015, **3**, 8262–8271.
- 86 G. J. Tattersall and W. K. Milsom, *J. Physiol.*, 2009, **587**, 5259–5274.